



Vibronic coherence and quantum beats of O_2^+ based on laser pump-probe dissociation dynamicsShan Xue ^{1,2} Shengjun Yue ^{1,2} Hongchuan Du,^{1,2,*} Bitao Hu,^{1,2} and Anh-Thu Le^{3,†}¹*School of Nuclear Science and Technology, Lanzhou University, Lanzhou 730000, China*²*Key Laboratory of Special Function Materials and Structure Design, Ministry of Education, Lanzhou University, Lanzhou 730000, China*³*Department of Physics, Missouri University of Science and Technology, Rolla, Missouri 65409, USA*

(Received 21 March 2021; accepted 21 June 2021; published 1 July 2021)

We report theoretical investigations of vibronic quantum beats (QBs) which can be observed in the molecular dissociation under the intense infrared (IR) laser pump-IR laser probe scheme. We show how the vibronic coherences can be probed by analyzing the interchannel QB signals obtained from the numerical solution of the time-dependent Schrödinger equation (TDSE) and the quantum Liouville equation in combination with the strong-field approximation for the treatment of coherences between multiple states of the target ion. The validities of our methods are first tested on a one-dimensional model of H_2^+ , for which exact solutions of the TDSE can be obtained. We then illustrate our method using an example of O_2 , for which various experiments have been reported recently. The case of an attosecond pump pulse is also considered. Our results indicate that the strong-field dissociation pump-probe experiments are capable of providing information on the vibronic coherences that complements other techniques such as attosecond transient absorption spectroscopy.

DOI: [10.1103/PhysRevA.104.013101](https://doi.org/10.1103/PhysRevA.104.013101)**I. INTRODUCTION**

After a set of molecular states is prepared coherently by laser ionization, ultrafast electronic and nuclear dynamics will occur on the timescales from attosecond to femtosecond [1–5]. Typically, the nuclear dynamics can be interrogated by the time-delayed ion signals with kinetic-energy-release (KER) distribution. By analyzing the KER and the quantum-beat (QB) spectra, vibrational dynamics have been investigated on the prototype molecule H_2 experimentally and theoretically [6,7], and the reconstruction of the potential energy curve (PEC) has also been achieved [8]. Here, the vibrational QBs are essentially derived from the coherences between the vibrational states within the same electronic state. Their frequencies are proportional to the energy gaps among these states. For more complex diatomic or polyatomic molecules, multiple electronic states are likely involved after photoionization [3,4,9–12]. The interference between these electronic states results in the so-called charge migration, a coherent oscillation of electron density with frequencies defined by their energy gaps. This (sub)femtosecond electronic motion induces subsequent rearrangements of atoms that could be responsible for chemical and biological reactions [13].

To initiate such ultrafast molecular dynamics after photoionization, it is necessary to ensure that there are sufficient ionic coherences established during the ionization process. The coherences between the electronic state play a crucial role in the attosecond molecular science [2–5]. Once the coherences are built up, ultrafast electronic dynamics occurs and

can be probed by using attosecond techniques, such as attosecond transient absorption spectroscopy (ATAS) [14]. However, the attosecond time resolution also exists in femtosecond infrared (IR) pulses, which is provided by their subcycle carrier-envelope-phase (CEP) effects. In this situation, two fundamental questions arise: (i) To what degree can the electronic coherences between ionic states be established upon photoionization in molecules? (ii) Are the (sub)femtosecond electronic coherences encoded in the pump-IR-probe signals, such as the KER spectra considered in this work, and if so, how?

In fact, the electronic coherence produced by photoionization has been studied extensively in atomic systems in both the linear and nonlinear regimes [15–18]. Atomic electronic coherence has even been reconstructed by using the ATAS in experiment [14]. For molecules, the preparation of the initial ionic wave functions after photoionization is a longstanding issue in theory. So far, it is still difficult to calculate the initial reduced density matrix (RDM) by a full *ab initio* method considering both the nuclear motion and photoionization simultaneously. As a simplified model, the sudden ionization is often used. Even with this initial pure state assumption, electronic decoherence still happens within a few femtoseconds in polyatomic molecules due to the interplay of multiple vibrational modes [19–21]. In the first part of this work, we investigate the quantum coherences generated by photoionization on simple diatomic molecules. The strong-field approximation (SFA) and perturbation theory models are adopted to prepare the initial RDM after ionization.

After photoionization, we take O_2 as an example to study the delay-dependent molecular dynamics and QB properties. Recently, Zhang *et al.* [22] presented a multi-reference configuration interaction (MRCI) study of the low-lying excited

*duhch@lzu.edu.cn

†lea@mst.edu

states of O_2^+ . The calculated spectra have reached a relatively accurate level when compared to the experimental results. In the study of molecular dynamics, Cörlin *et al.* [23] adopted the attosecond pulse train (APT)-pump-IR-probe scheme. They primarily detected the $a^4\Pi_u$ -state vibrational QBs of 0.104 eV (25.1 THz) with $E_{KER} < 0.8$ eV. These QBs originate from the vibrational nuclear wave packet in the ionic $a^4\Pi_u$ PEC created by the pump ionization, followed by its dissociation through the $f^4\Pi_g$ state by absorbing a photon from the probe pulse. A similar attempt was made by De *et al.* in an IR-pump-IR-probe scheme [11,24]. They predominantly observed the 32-THz QBs. Recent work confirmed that these QBs originated from the ionic $b^4\Sigma_g^-$ state [25]. The resonant coupling between states $a^4\Pi_u$ and $b^4\Sigma_g^-$ during the pump efficiently increases the population of the $b^4\Sigma_g^-$ state, so the $b^4\Sigma_g^-$ -state vibrational QBs dominate in the spectrum. More interestingly, there are separated high-frequency QBs near 1.5 eV, which are proportional to the energy gaps between the $a^4\Pi_u$ and $b^4\Sigma_g^-$ states. In the following, these QBs will be called electronic-vibronic (vibronic) QBs. So far, no high-frequency vibronic QBs have been reported in experiments. The problem may be caused by either weak vibronic coherences generated by the pump ionization or insufficient time resolution of the delayed probe pulses. In the second part of this work, we explore the possibility to observe the vibronic QBs and investigate the properties of these signals.

The paper is organized as follows. In Sec. II, we describe the time-dependent quantum methods, the ionic PECs, and the ionization rates under two ionization mechanisms. Our results are presented in Sec. III. In Sec. III A, we investigate the quantum coherences generated by photoionization. The theoretical models are tested on a one-dimensional H_2 system. In Sec. III B, we investigate the vibronic QBs of O_2^+ in the probing of IR pulses. The properties, angular distribution, and frequency shifts of the QBs, respectively, are discussed. Our conclusion is summarized in Sec. IV. Atomic units are used throughout the paper, unless otherwise indicated.

II. THEORETICAL APPROACH

A. Time-dependent quantum methods and evaluation of quantum coherence

The rotational period of O_2 is about 11.6 ps, which is much longer than the pulse duration and the pump-probe time delay (500 fs) used in our calculation. It is therefore safe to assume that the molecular axis is fixed in space. For an initial ionic pure state after the pump ionization, we solve the coupled-channel time-dependent Schrödinger equation (CCTDSE). For an initial mixed state, we solve the quantum Liouville equation (QLE). These two methods give the same results for an initial pure state in our calculations.

1. Coupled-channel time-dependent Schrödinger equation

By expanding the total wave function in the Born-Oppenheimer (BO) electronic states, the CCTDSE for the

channel wave functions $\chi_m(R, t)$ is expressed as

$$i\frac{\partial}{\partial t} \begin{pmatrix} \chi_1 \\ \chi_2 \\ \vdots \end{pmatrix} = \begin{pmatrix} T_R + V_1 & \mathbf{E}_{(\text{probe})}(t) \cdot \mathbf{u}_{12} & \dots \\ \mathbf{E}_{(\text{probe})}(t) \cdot \mathbf{u}_{21} & T_R + V_2 & \dots \\ \vdots & \vdots & \ddots \end{pmatrix} \times \begin{pmatrix} \chi_1 \\ \chi_2 \\ \vdots \end{pmatrix}, \quad (1)$$

where $V_m(R)$ is the adiabatic BO potential of channel m with the internuclear distance R , $\mathbf{u}_{mn}(R)$ is the transition dipole matrix element between channels m and n , and $T_R = -\frac{1}{2\mu}\partial^2/\partial R^2$ is the nuclear kinetic-energy operator with the nuclear reduced mass μ . $\mathbf{E}_{(\text{probe})}(t)$ is the electric field of the probe pulse,

$$E_{(\text{probe})}(t) = E_0 e^{-2\ln(2)[(t-t_d)/\tau]^2} \cos(\omega t + \phi), \quad (2)$$

where τ is the full width at half maximum (FWHM), E_0 is the electric field amplitude, and ω is the laser frequency. t_d is the delay time. ϕ is the carrier-envelope phase (CEP), which is set to be 0 in our calculation. The pump light is in the same Gaussian-envelope form, but centered at time 0. The CCTDSE is solved using the Crank-Nicolson method [25]. We typically use a spatial step of $\Delta R = 0.01$ a.u. and propagate up to $R_{\text{max}} = 30$ a.u. with the time step $\Delta t = 2.5$ a.u. The wave function is propagated for another three to six cycles after the end of the probe pulse to ensure that the low-energy dissociation signals are collected. The momentum representations of the dissociation signals at delay time t_d are then calculated by Fourier transforming the dissociating part of the wave packets at the end of the propagation t_{max} ,

$$\tilde{\chi}_m^{\text{dis}}(P, t_d) = \int dR \chi_m^{\text{dis}}(R, t_{\text{max}}) e^{iPR}. \quad (3)$$

By incoherently adding the momentum distributions from all electronic states, one obtains the delay-dependent KER spectrum by

$$C^{\text{dis}}(E_k, t_d) = \sum_m |\tilde{\chi}_m^{\text{dis}}(P, t_d)|^2 / P. \quad (4)$$

For homonuclear molecules, $E_k = P^2/(2\mu)$.

2. Quantum Liouville equation

The density operator for a mixed state reads

$$\hat{\rho} = \sum_k P_k |\Phi_k\rangle \langle \Phi_k|, \quad (5)$$

where P_k represents the probability that the ionic system is in a pure state Φ_k . Under the BO approximation, the density matrix can be expressed in terms of the vibronic states, $\rho_{ij}^{mn} = \langle \psi_m \chi_i^m | \hat{\rho} | \psi_n \chi_j^n \rangle$. Here and in the following, indices m and n are used to denote the electronic states; indices i, j represent the vibrational state in the m th and n th PECs. For example, $\chi_i^m(R)$ is the i th vibrational state of the electronic state $\psi_m(\mathbf{r}; R)$, where \mathbf{r} represents the electronic coordinates. Unitary evolution of the density matrix is described by the

QLE,

$$i\frac{\partial}{\partial t}\rho_{ij}^{mn} = (E_i^m - E_j^n)\rho_{ij}^{mn} - \mathbf{E}(t) \cdot \sum_{o,l} (\mathbf{u}_{il}^{mo}\rho_{lj}^{on} - \rho_{il}^{mo}\mathbf{u}_{lj}^{on}), \quad (6)$$

where $\mathbf{u}_{ij}^{mn} = \langle \chi_i^m | \mathbf{u}_{mn}(R) | \chi_j^n \rangle$ is the electric dipole matrix element. Here, we ignore the decoherence factors such as predissociation and spontaneous radiation on a typically nanosecond to microsecond timescale [26,27] since the total delay time is only several-hundred femtoseconds. The QLE is integrated by using the fourth-order Runge-Kutta method with a time step $\Delta t = 2.5$ a.u. The dissociative eigenstates are obtained by diagonalizing the Hamiltonian in the coordinate space. We choose the dissociation energy up to 2 eV to include most of the dissociation signals under current laser parameters. Then the delay-dependent KER spectrum can be calculated by

$$C^{\text{dis}}(E_k, t_d) = \sum_m \rho_{\text{dis}}^{mm}(E_k) / P. \quad (7)$$

Here, $\rho_{\text{dis}}^{mm}(E_k)$ is the population of the dissociative state on the m th PEC.

Once the delay-dependent KER spectrum is obtained by either the CCTDSE or QLE, the QB spectrum in the KER-frequency space can be calculated by

$$P^{\text{dis}}(E_k, f) = \left| \int dt_d C^{\text{dis}}(E_k, t_d) e^{-i2\pi f t_d} \right|. \quad (8)$$

3. Evaluation of quantum coherence

The off-diagonal element ρ_{ij}^{mn} of the RDM represents the vibronic coherence. When the decoherence effect is not considered, $|\rho_{ij}^{mn}|$ will remain unchanged after the pump pulse. The R -dependent electronic coherence is expressed as

$$\rho_{mn}(R, t) = \sum_{ij} \rho_{ij}^{mn}(t_f) e^{-i\omega_{ij}^{mn}(t-t_f)} \chi_i^m(R) \chi_j^n(R), \quad (9)$$

where $\omega_{ij}^{mn} = E_i^m - E_j^n$, t_f is the end time of the pump pulse. The total electronic coherence $\rho_{mn}^{\text{tot}}(t)$ can be obtained by integrating over R . For diatomic molecules, the evolution of $|\rho_{mn}^{\text{tot}}|$ is mainly attributed to the motions of the one-dimensional nuclear wave packets at different PECs. The degree of coherence (DOC) between two vibrational states is given by $g_{ij}^{mn} = |\rho_{ij}^{mn}| / \sqrt{\rho_{ii}^{mm}\rho_{jj}^{nn}}$, whose value varies from 0 to 1. The larger the value, the higher the DOC.

B. Potential energy curves

The low-energy KER and QB spectra of O_2^+ in the experiments can be quantitatively reproduced by using the three-state model containing the $a^4\Pi_u$, $b^4\Sigma_g^-$, and $f^4\Pi_g$ states [23,25]. Since the laser parameters used in the present work are similar to those in the experiments [11,23,24], we adopt the same three-state model in the following.

To obtain accurate QB positions, we use the Rydberg-Klein-Rees (RKR) PECs for states $a^4\Pi_u$ and $b^4\Sigma_g^-$. They are generated by the program RKR1 [29] with the vibrational parameters given by the MRCI calculation in Ref. [22]. For the dissociative $f^4\Pi_g$ state, the PEC reported by Marian *et al.* [28] is adopted. It leads to the result that the calculated KER spec-

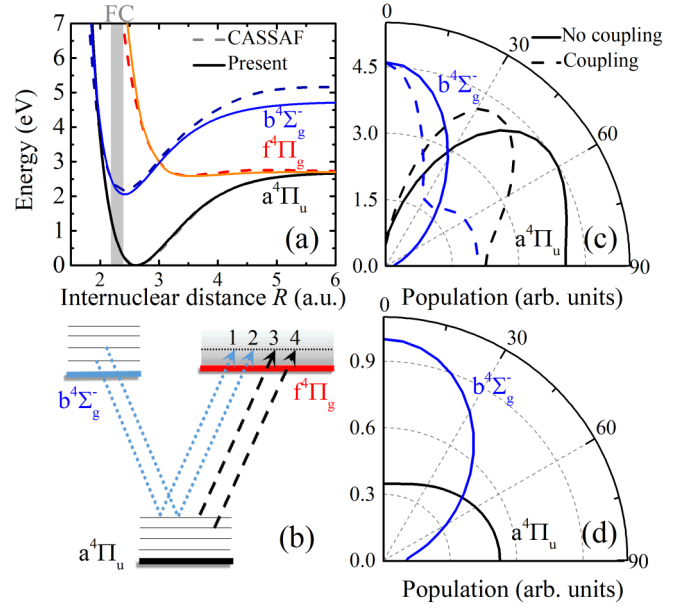


FIG. 1. (a) O_2^+ PECs for main channels included in the simulations. $f^4\Pi_g$ curve from Marian *et al.* [28] and RKR potentials of $a^4\Pi_u$ and $b^4\Sigma_g^-$ are shown as solid lines. PECs calculated from CASSCF are shown as dashed lines. (b) Sketch of the QB pathways. Paths 1 and 2, and 3 and 4 contribute to the vibrational QB; paths 1 and 3, 1 and 4, 2 and 3, and 2 and 4 contribute to the vibronic QBs. (c) Polar plot of angle-dependent populations of $a^4\Pi_u$ and $b^4\Sigma_g^-$ ionized from O_2 , obtained by the MO-ADK theory at the intensity of 1.5×10^{14} W/cm² with and without the dipole coupling effect. (d) Polar plot of angle-dependent populations for the XUV pump pulse with the photon energy 17–40 eV [23].

tra below 0.1 eV are in good agreement with the experimental results [30]. Figure 1(a) shows the PECs of these three states. The PECs calculated from the complete active space multiconfigurational self-consistent field (CASSCF) method are also presented for comparison. The parallel and perpendicular transition dipole moments of $a^4\Pi_u-f^4\Pi_g$ and $a^4\Pi_u-b^4\Sigma_g^-$ calculated by the CASSCF method are adopted. More details of the CASSCF method can be found in Ref. [25].

C. Ionization rate

We use the SFA and perturbation theory models to prepare the RDM during the pump pulse, in which the ionization rates are required.

For the tunneling ionization case, the angle-dependent ionization rates are calculated within the molecular Ammosov-Delone-Krainov (MO-ADK) theory [31], as shown by the solid lines in Fig. 1(c). The ionic $a^4\Pi_u$ and $b^4\Sigma_g^-$ states are produced by removing the electrons from the HOMO-1 and HOMO-2 orbitals of O_2 , respectively. Their vibrational distributions are modeled by the Franck-Condon (FC) factors. Without considering the resonant coupling effects, the initial populations of the vibronic states are proportional to the products of the MO-ADK rates and the FC factors. By taking into account the resonant coupling between $a^4\Pi_u$ and $b^4\Sigma_g^-$ during the pump pulse, the populations of these two states change significantly, as shown by the dashed lines in Fig. 1(c)

(see, also, Ref. [25]). Specific calculation details are given in Sec. III A 1.

For the extreme ultraviolet (XUV) single-photon ionization, the angle-dependent ionization rate of O_2 is modeled by using the differential cross section σ_m and the molecular orientation parameter β_m given in Ref. [32]. By integrating within the bandwidth of the XUV pulse $f(\omega)$, the ionization rate to the ionic state m reads $\Gamma_m^{(XUV)}(\theta) = \int d\omega |f(\omega)|^2 \sigma_m(\omega) [1 + \beta_m(\omega) P_2(\cos\theta)]$. Here, $P_2(\cos\theta)$ is the second-order Legendre polynomial, and θ is the angle between the polarization direction and the molecular axis. The calculated results are shown in Fig. 1(d). FC factors are used for the vibrational-state distribution.

III. RESULTS AND DISCUSSION

A. Quantum coherence induced by photoionization

Molecular dynamics after photoionization essentially depends on the quantum coherences established during the ionization process. A necessary condition for the coherence to build up is that electrons of different ionization orbitals are ionized into the same continuum state [18,33]. In order to evaluate the quantum coherences after photoionization, we adopt the SFA and perturbation theory models to calculate the initial RDM of homonuclear diatomic molecules. Strong IR pulse and APT are considered as the pump pulses since they have been used in the experiments on O_2 [11,23,24]. We then test the validities of the models on a one-dimensional H_2 system by comparing with the TDSE results.

1. Case of the IR pump pulse

For intense IR pump pulses, the ionization mechanism is mainly tunneling ionization. Recently, Pabst *et al.* [17] proposed an intuitive model based on the SFA to prepare the initial RDM generated by the intense IR pulse. The results calculated by the model are in good agreement with those calculated by the time-dependent configuration interaction singles (TDCIS) method on atomic xenon. We therefore extend this model to the case of homonuclear diatomic molecules. With multiple vibronic states involved, the RDM reads

$$\rho_{ij}^{mn}(t_f) = \int_{-\infty}^{t_f} dt \sqrt{\Gamma_i^m \Gamma_j^n} \text{sgn}[E_{\text{pump}}(t)]^{(2-P_m-P_n)/2} e^{i\omega_{ij}^{mn}(t_f-t)}. \quad (10)$$

Here, $\Gamma_i^m[E_{\text{pump}}(t)] = \Gamma_m^{(\text{ADK})}[E_{\text{pump}}(t)] |c_i^{m(\text{FC})}|^2$ is a multiplication of the tunneling ionization rate at the equilibrium R_e and the FC factors. It represents the transient ionization rate to the vibronic state v_i^m at every instant during the pump pulse. $P_{m(n)}$ describe the inversion symmetries of the ionization orbitals with 1(−1) representing the $g(u)$ symmetry. Equation (6) can be interpreted as follows. At each ionization moment, a pure state is populated according to the ionization rate, then propagates freely. Finally, these pure states are superimposed at the final time t_f so that a mixed state is built. In fact, after each ionization event, the wave packet is still under the influence of the residual pump field. Thus the laser coupling effect cannot be ignored [25,34]. To account for this effect, we prepare the initial vibronic state at each ioniza-

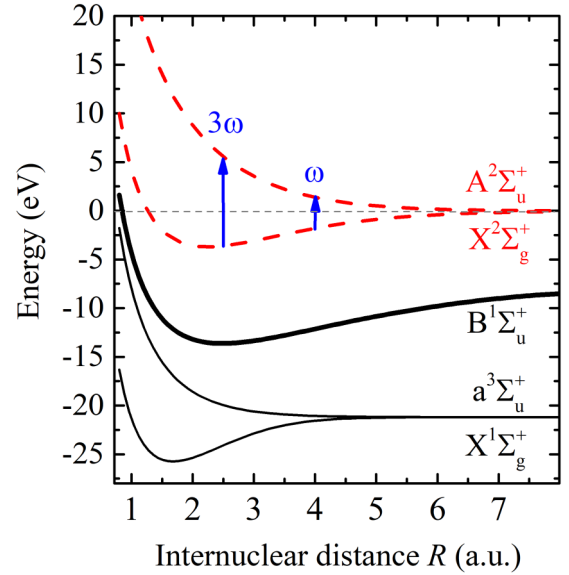


FIG. 2. PECs of H_2^+ (dashed lines) and H_2 (solid lines). For electronic coordinates x_1, x_2 , the spatial molecular orbital configurations of H_2 are $X^1\Sigma_g^+$: $1\sigma_g(x_1)1\sigma_g(x_2)$; $a^3\Sigma_u^+$: $1\sigma_g(x_1)1\sigma_u(x_2) - 1\sigma_u(x_1)1\sigma_g(x_2)$; $B^1\Sigma_u^+$: $1\sigma_g(x_1)1\sigma_u(x_2) + 1\sigma_u(x_1)1\sigma_g(x_2)$ [35].

tion moment by $c_{i(j)}^{m(n)}(t) = \sqrt{\Gamma_{i(j)}^{m(n)}} \text{sgn}[E_{\text{pump}}(t)]^{[1-P_{m(n)}]/2}$, and propagate the nuclear wave packet in the residual pump field by solving the CCTDSE. At the end of the pump pulse, the RDM reads $\rho_{ij}^{mn} = \int_{-\infty}^{t_f} dt c_i^m(t_f, t) c_j^{n*}(t_f, t)$, where $c_i^m(t_f, t)$ is the vibronic-state amplitude at t_f .

To test the validity of the model, we compare the calculated results of the SFA model and TDSE on the one-dimensional H_2 system. In the system, the two electrons and nuclei are restricted to move along the laser polarization direction. Here, the TDSE deals with all the nuclear and electronic degrees of freedom. It is different from the CCTDSE treatment described in Sec. III A 1, which couples several ionic PECs without considering the ionized electron. Details of the H_2 model and the TDSE method can be found in Ref. [35]. The PECs of H_2 and H_2^+ are shown in Fig. 2. For an analogy of multi-orbital ionization of complex molecules, the second-excited state $B^1\Sigma_u^+$ is set to be the initial state of H_2 . It contains only two molecular orbitals. The removal of the electron from the HOMO ($1\sigma_u$) or HOMO-1 ($1\sigma_g$) orbital results in the ground ($X^2\Sigma_g^+$) or excited ($A^2\Sigma_u^+$) states of H_2^+ .

Figure 3 presents the DOCs between the vibronic states of $X^2\Sigma_g^+$ and $A^2\Sigma_u^+$ calculated by the SFA and TDSE. In our calculation, three-cycle 400-nm pump pulses at two laser intensities are used. For the vibronic coherence, as shown in Figs. 3(a)–3(d), the calculated results of both methods are coincident in predicting the local maxima at around $\omega_{ij}^{ab} = \omega$ and 3ω , shown as gray lines for comparison. Note that ω is the circular frequency of the pump pulse. Moreover, it is found that the lower the laser intensity, the better the consistency. The formation of the local maxima can be understood in the following two aspects: (i) Considering two pure states populated at adjacent field crests, denoted as $\rho_{ij}^{ab(1)}$ and $\rho_{ij}^{ab(2)}$, only the vibronic-state pairs with $\omega_{ij}^{ab} \approx (2n+1)\omega$ can accumulate phase differences around $2n\pi$ at the end of the pump since

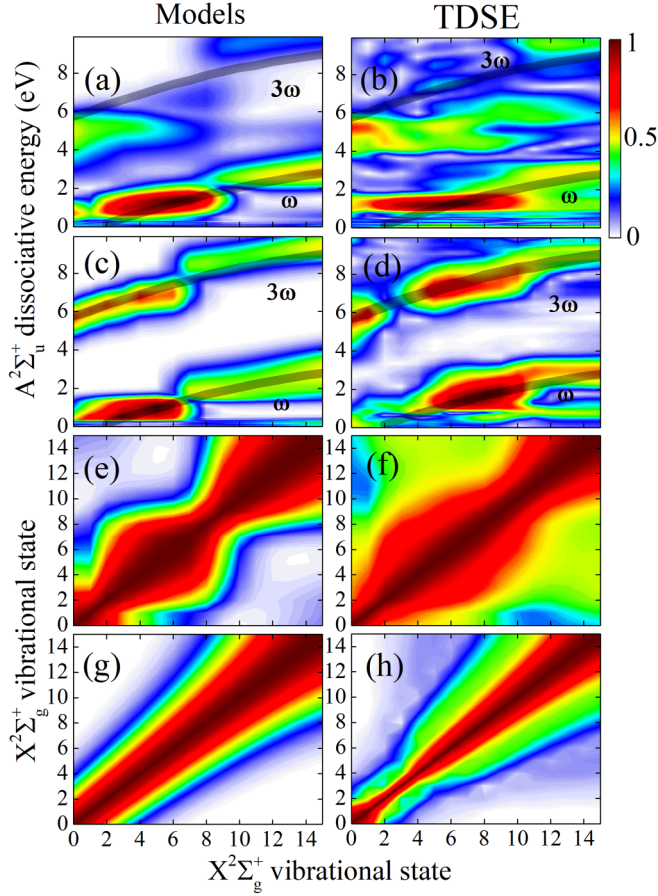


FIG. 3. The degrees of coherences of H_2^+ . Left panels represent the results from the SFA and perturbation theory models; right panels are the results of the TDSE. (a), (b) The degrees of the vibronic coherences g_{ij}^{ab} between the vibronic states on the $X^2\Sigma_g^+$ and $A^2\Sigma_u^+$ PECs prepared by a three-cycle 400-nm pump pulse with an intensity of $3 \times 10^{14} \text{ W/cm}^2$. The vibronic states on the $A^2\Sigma_u^+$ PEC are labeled by their dissociative energies. (c), (d) Same as (a), (b), but with an intensity of $3 \times 10^{13} \text{ W/cm}^2$. (e), (f) The degrees of the $X^2\Sigma_g^+$ -state vibrational coherences induced by IR pulse with an intensity of $3 \times 10^{14} \text{ W/cm}^2$. (g), (h) The degrees of the $X^2\Sigma_g^+$ -state vibrational coherences induced by a 2.7-fs APT pulse.

the parities of the two ionization orbitals are opposite. (ii) The ω and 3ω resonant transition between $X^2\Sigma_g^+$ and $A^2\Sigma_u^+$ in the residual pump field will introduce new coherences to the vibronic-state pairs. Therefore, we conclude that the local maxima of the vibronic coherences are associated to the circular frequency, namely, the wavelength of the pump pulse.

At the lower intensity, the local maxima look more regular and show better circular-frequency dependence, as shown in Figs. 3(c) and 3(d). This means that it is more reliable to manipulate the coherent region by photoionization according to the pump wavelength. However, we find that the $A^2\Sigma_u^+$ -state population is two orders smaller than that of the $X^2\Sigma_g^+$ -state in this case. This may lead to very weak delay-dependent vibronic oscillations in the following detection. Whereas for the strong IR pump, the resonant transition from $X^2\Sigma_g^+$ to $A^2\Sigma_u^+$ makes the populations of the two states comparable and also provides certain vibronic coherence. This could lead

to a better signal-to-noise ratio of the vibronic QBs in the experimental measurement. However, the downside is that the coherent local maxima exhibit less circular-frequency dependence under such strong pump intensity, as shown in Fig. 3(b). The discrepancies between the local maxima and the gray lines may be attributed to the distortion of the ionic PECs under the strong laser field. In this case, laser-induced adiabatic states should be considered as the basis sets in the process of building up the vibronic coherences. The distortion of the PECs and the transition probabilities depend on the strength of the transition dipole moment and the energy gaps between the electronic states. Therefore, the situations may be different for other molecular systems. For example, for O_2 , discussed in the next section, good control of the wavelength-dependent coherent region and clear signal contrast can both be realized under the strong IR pump pulse.

For the vibrational coherence, Figs. 3(e) and 3(f) show the $X^2\Sigma_g^+$ -state vibrational DOCs. The model reproduces the TDSE results in which the coherence decreases with Δv . When $\Delta v = 1$, extremely small energy gaps make the last exponential term in Eq. (6) approximately equal to 1. However, as the energy gap increases, i.e., $\Delta v > 1$, the coherent condition is gradually destroyed, leading to the rapid decreasing of the DOC. In conclusion, the SFA model captures the main features of the TDSE results. The model is applied to homonuclear diatomic molecules but can also be extended to polyatomic molecules with inversion symmetry.

2. Case of the APT pump

For the weak APT pump, the ionization mechanism is mainly single-photon ionization. Based on the first-order perturbation theory, we develop a model to evaluate the initial RDM.

Typically, attosecond pulses radiate every half cycle. Then the APT can be written as

$$E_{\text{APT}}(t) = f_{\text{APT}}(t) \left[\sum_k E_{\text{SAP}}(t - t_k) e^{i\phi_k} \right], \quad (11)$$

where $f_{\text{APT}}(t)$ is the Gaussian envelope of the APT. $E_{\text{SAP}}(t - t_k)$ is the single attosecond pulse centered at t_k . ϕ_k represents the CEP of each attosecond pulse. Based on the perturbation theory, the ionization amplitude from the neutral state to the ionic vibronic state v_i^m accompanied by a photoelectron with momentum \mathbf{v} is given by

$$\begin{aligned} M_i^m(\mathbf{v}) &= i \int_{-\infty}^{t_f} dt D_i^m(\mathbf{v}) E_{\text{APT}}(t) e^{i(\mathbf{v}^2/2 + E_i^m)(t - t_f)} \\ &\approx \sum_k f_{\text{APT}}(t_k) i \int dt D_i^m(\mathbf{v}) E_{\text{SAP}}(t) e^{i(\mathbf{v}^2/2 + E_i^m)t} \\ &\quad \times e^{i(\mathbf{v}^2/2 + E_i^m)(t_k - t_f)} e^{i\phi_k} \\ &= \sum_k f_{\text{APT}}(t_k) m_i^m(\mathbf{v}) e^{i(\mathbf{v}^2/2 + E_i^m)(t_k - t_f)} e^{i\phi_k}, \quad (12) \end{aligned}$$

where $D_i^m(\mathbf{v}) = \langle \chi_i^m | u_{m,\text{neu}}(\mathbf{v}; R) | \chi_g^{\text{neu}} \rangle_R$ represents the dipole matrix element between the neutral vibrational state and the ionic vibronic state accompanied by the photoelectron with momentum \mathbf{v} . $u_{m,\text{neu}}(\mathbf{v}; R)$ is the ionization transition dipole moment element at each R . $m_i^m(\mathbf{v})$ is the ionization amplitude

for a single attosecond pulse. The integral over time in the above formula is decomposed into the time integral for each attosecond pulse.

After tracing out the degree of freedom of the unobserved photoelectron, the RDM of the ion is given by

$$\begin{aligned}
 \rho_{ij}^{mn} &= \int d\mathbf{v} M_i^m(\mathbf{v}) M_j^{n*}(\mathbf{v}) \\
 &\approx \sum_k f_{\text{APT}}^2(t_k) \left| \int m_i^m(\mathbf{v}) m_j^{n*}(\mathbf{v}) d\mathbf{v} \right| e^{i\delta} e^{i\omega_{ij}^{mn}(t_k - t_f)} \\
 &\approx \frac{|P_m + P_n|}{2} \sum_k f_{\text{APT}}^2(t_k) \sqrt{\Gamma_i^m(\text{XUV})(t_k) \Gamma_j^n(\text{XUV})(t_k)} \\
 &\quad \times e^{i\delta} e^{i\omega_{ij}^{mn}(t_k - t_f)}. \tag{13}
 \end{aligned}$$

The electronic wave packets emitted at different times have small overlap due to the rapid spreading of wave packets in the continuum, so we neglect the terms that two ionic states are populated at different times. In the derivation above, we also use the sudden ionization assumption, i.e., $\int m_i^m(\mathbf{v}) m_j^{n*}(\mathbf{v}) d\mathbf{v} \approx e^{i\delta} \frac{|P_m + P_n|}{2} \sqrt{\int |m_i^m(\mathbf{v})|^2 d\mathbf{v} \int |m_j^n(\mathbf{v})|^2 d\mathbf{v}}$. Here, δ is the phase of the integral. The ionization rate to v_i^m is replaced by Γ_i^m , which is the product of the XUV ionization rate at the equilibrium geometry and the FC factors. $\frac{|P_m + P_n|}{2}$ reflects the effect of the orbital symmetry. When two ionization orbitals have opposite inversion symmetries, the electrons from these two orbitals cannot be ionized into continuum states with the same symmetry upon one-photon absorption [14–18]. Thus there is no vibronic coherence between the two electronic states. In our case, the ionization orbitals HOMO($1\sigma_u$), HOMO-1($1\sigma_g$) for $B^1\Sigma_u^+$ of H_2 , and HOMO-1($3\sigma_g$), HOMO-2($1\pi_u$) for $X^3\Sigma_g^-$ of O_2 , satisfy this situation. Equation (9) can be interpreted as follows: At each attosecond pulse burst, ionic pure states are populated according to the ionization rates and propagate freely; finally, these states are superimposed to produce the mixed state.

To test the validity of this model, we compare the results for H_2 with the exact ones of the TDSE. A 2.7-fs Gaussian-envelope APT is used in the calculation and adjacent pulses are separated by half cycle of the 400-nm pulse and out of phase by π . It is found that there is indeed no vibronic coherence in the results from the two methods. Only the vibrational coherences are generated in each electronic state. Figures 3(g) and 3(h) show the vibrational DOCs of the $X^2\Sigma_g^+$ state. The calculated results of the model reproduce the features of the TDSE results, namely, the vibrational DOC decreases with Δv . Similar to the IR case, this is because the periodic ionization bursts that happen during the APT pulse gradually destroy the coherent condition when $\Delta v > 1$.

It should be pointed out that this model is based on the sudden ionization assumption and focuses on the periodic time effects of the ionization bursts on the building up of the quantum coherences. In other words, the populated ionic wave packet is assumed to be a pure state upon ionization of each attosecond pulse. Then the coherences are built up by adding up the density matrices of these pure states at the end of the APT. In this aspect, our model cannot assess the ionic coherences produced by the ionization of a single attosecond pulse. For the single pulse case, Pabst *et al.* [16] found that perfectly

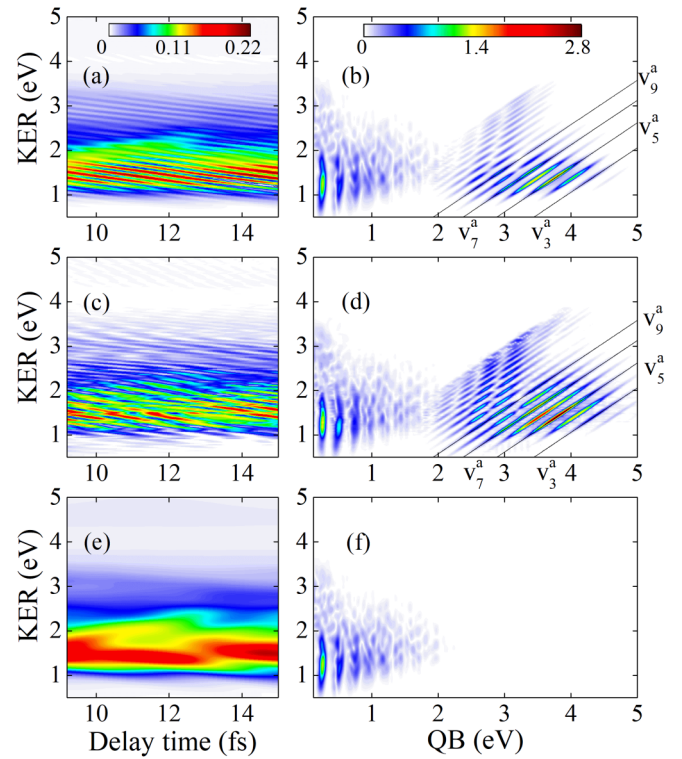


FIG. 4. (a) Delay-dependent KER spectrum of H^+ detected by a 400-nm three-cycle probe pulse with an intensity of $1 \times 10^{14} \text{ W/cm}^2$. The RDM calculated by the TDSE is adopted as the initial condition. (b) Corresponding QB spectrum. (c), (d) Same as (a), (b), but with an initial pure state condition. (e), (f) Same as (a), (b), but setting the initial vibronic coherences to 0.

coherent hole wave packets can hardly be formed even with sufficiently large spectral bandwidth. Perfect coherence can only be approached by increasing the mean photon energy of the XUV pulse. Considering these effects of a single pulse, the overall ionic coherences estimated by our perturbation theory model in the APT case will decrease accordingly. But the features of the DOCs influenced by the periodic time effects will not change.

3. Effect of quantum coherence on QB

With the quantum coherences generated by the pump pulses, we investigate how the coherences are encoded in the delay-dependent dissociation signals in this section. Taking the DOCs shown in Fig. 3(b) as the initial condition, we calculate the delay-dependent KER and QB spectra by solving the QLE. The results are shown in Figs. 4(a) and 4(b). The QBs in the range of ~ 0 – 1 eV come from the $X^2\Sigma_g^+$ -state vibrational coherences; and the QBs within ~ 2 – 4.5 eV come from the vibronic coherences between the $X^2\Sigma_g^+$ and $A^2\Sigma_u^+$ states. The vibronic QBs essentially result from the interferences between the direct dissociation paths of $A^2\Sigma_u^+$ and indirect dissociation paths from $X^2\Sigma_g^+$ to $A^2\Sigma_u^+$. Their frequencies correspond to the vibronic-state energy gaps, which are marked as solid lines in the QB spectrum. For states $\sim v_2^g$ – v_3^g , the local maxima shown in Fig. 3(b) are mainly located around the dissociative energy of ~ 0.7 – 1.8 eV. This

is reflected in the QB spectrum shown in Fig. 4(b), in which intense vibronic QBs appear within this range.

To further illustrate the influence of quantum coherence on the QB, we also present the results under the pure state condition and under the condition of ignoring the vibronic coherences in Figs. 4(c), 4(d) and Figs. 4(e), 4(f) respectively. For an initial pure state, the QBs are overall stronger than those of the mixed state in Fig. 4(b). In particular, there exist relatively strong vibronic QBs at $E_{\text{KER}} > 1.8$ eV. Conversely, by setting the vibronic coherences to zero, the vibronic QBs disappear in Fig. 4(f). This indicates that the QB strength is directly linked to the quantum coherence.

In the case of H_2^+ , the total electronic coherence will disappear within several femtoseconds due to the decay of the nuclear wave-packet overlap. However, the vibronic coherences can still be observed in the QB spectrum. Our results imply that the vibronic coherence plays a more fundamental role than the electronic coherence in molecular dynamics. The delay-dependent KER spectra can also be calculated using a full solution of the TDSE considering both the pump and probe lasers, but with high computational costs. It has been verified that the main results remain unchanged under the full solution of the TDSE.

B. QB properties on O_2^+

Based on the theoretical models described in the previous section, the initial RDM after photoionization can be calculated for homonuclear diatomic molecules. In this section, we take O_2 as a practical example to study the quantum coherences generated by photoionizations and the subsequent molecule dynamics. In the three-state model, the vibrational wave packets are first populated on the $a^4\Pi_u$ and $b^4\Sigma_g^-$ PECs after the pump ionization, followed by dissociation through the $a^4\Pi_u-f^4\Pi_g$ transition by interacting with the probe pulses. The QB spectrum is then obtained from the Fourier transforming of the delay-dependent dissociation signals for the sampling time of 500 fs. The pathways of the QBs on O_2^+ are depicted schematically in Fig. 1(b). The vibrational QB is associated with the interference between two vibrational states on the same PEC; the vibronic QB is associated with the vibrational states on different PECs that contribute to the same dissociative state.

In the calculations, the polarizations of the pump and probe pulses are parallel. Signals are detected from different angles, which designate the orientation of the molecular axis relative to the polarization direction. We take the angle of 45° as an example to illustrate the quantum coherences and QBs in the following, unless otherwise stated.

1. QBs upon initial pure state

We first investigate the QB properties for an initial pure state. The initial populations of the vibronic states are modeled by the MO-ADK theory and the FC factors. The wavelength and intensity of the probe pulse are 760 nm and 3×10^{12} W/cm², which are the same as the experiment of Cörlin *et al.* [23] except for the pulse duration.

Figure 5 shows the delay-dependent KER and QB spectra for the 35-fs and 15-fs probe pulses. In the KER spectra, there are both signal oscillations with tens of femtoseconds and fine

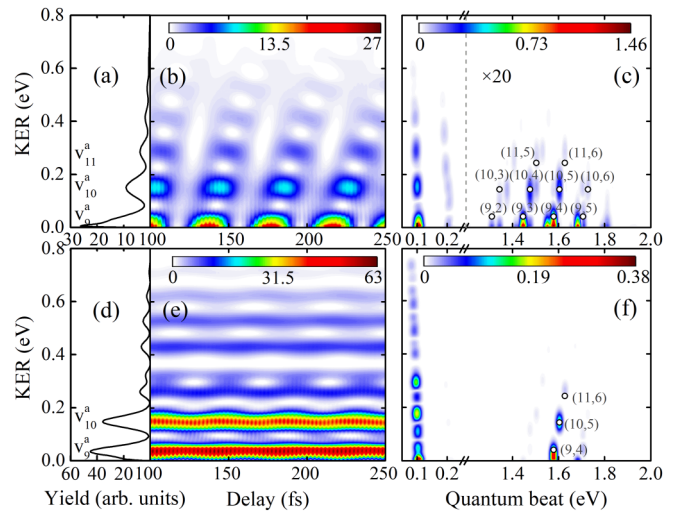


FIG. 5. (a) Averaged and (b) delay-dependent KER spectra for a 15-fs 760-nm probe pulse with an intensity of 1×10^{12} W/cm². The results are calculated by the CCTDSE method with a pure state as the initial condition. (c) The QB spectrum of the delay-dependent signals. The amplitudes of the vibronic QBs from 1.2 to 2.0 eV are magnified 20 times for a better presentation. Predicted positions of the vibronic QBs are shown as white circles. (d)–(f) are the same as (a)–(c), but for a 35-fs probe pulse.

structures of a few femtoseconds, which correspond to the low-frequency vibrational QBs and high-frequency vibronic QBs, respectively. For the vibrational QBs, the frequencies around 0.105 and 0.207 eV originate from the $a^4\Pi_u$ -state vibrational coherences with $\Delta v = 1$ and $\Delta v = 2$. Their frequency locations are almost identical to the experimental results of Cörlin *et al.* [23], in which the locations are reported around 0.104 eV with $E_{\text{KER}} < 0.05$ eV for $\Delta v = 1$. We find that the 0.105-eV QB originates from the vibrational-state pair (v_8^a, v_9^a), and it is mainly the v_9^a state that leads to the first KER peak by absorbing one photon from the probe pulse. For the vibronic QBs, the frequencies near 1.6 eV correspond to the coherences between $a^4\Pi_u$ and $b^4\Sigma_g^-$ with energy differences around ω . For comparison, we also provide the predicted positions for the vibronic QBs, shown as open circles and labeled (v_i^a, v_j^b). Their horizontal coordinates correspond to the vibronic energy differences, and vertical coordinates are calculated according to the energy conservation, i.e., one-photon transition from $a^4\Pi_u$ to $f^4\Pi_g$. Obviously, the frequency positions of the vibronic QBs agree with the predicted ones. Moreover, they do not change as the parameters of the probe pulses vary (see, also, Ref. [25]). Therefore, these vibronic QBs provide a feasible way to calibrate the vibronic-state energies and to reconstruct the related PECs.

Next, we discuss the influence of the duration of the probe pulse on the QB spectrum. For the 35-fs probe pulse, the long duration effectively enhances the $b^4\Sigma_g^- - a^4\Pi_u$ transition, but has bad time resolution for the vibrational oscillations of around 40 fs. Therefore, strong vibronic QBs and weak vibrational QBs show up in Fig. 5(f). For example, at $E_{\text{KER}} \approx 0.05$ eV, the depth of the fine-structure oscillation (vibronic oscillations of a few femtoseconds) is about 25% of the background signal. We believe that such a strong signal contrast

can be observed in the experimental measurement. However, for the 15-fs probe pulse, the short duration makes the vibrational QBs stronger but the vibronic QBs weaker, as shown in Fig. 5(c). Moreover, the wide bandwidth of the short probe pulse covers the gaps of multiple vibronic-state pairs, so more vibronic QBs show up in Fig. 5(c).

To better understand the nature of the vibronic QB, we simplify the $a^4\Pi_u-b^4\Sigma_g^-$ transition during the probe pulse by using the first-order perturbation theory. Then the delay-dependent v_i^a -state population after the probe pulse reads

$$|c_i^a(t = \infty; t_d)|^2 \approx |c_i^{a(0)}|^2 + \sum_j 2\mathbf{u}_{ij}^{ab} |\tilde{\mathbf{E}}(\omega_{ij}^{ab}) c_i^{a(0)} c_j^{b(0)}| \times \sin(\omega_{ij}^{ab} t_d - \phi + \delta_j^b - \delta_i^a), \quad (14)$$

where $c_{i(j)}^{a(b)(0)}$ is the initial complex amplitude with the initial phase $\delta_{i(j)}^{a(b)}$. $\omega_{ij}^{ab} = E_j^b - E_i^a$ is the vibronic energy difference. $\tilde{\mathbf{E}}(\omega)$ is the frequency component of the probe electric field. The oscillating v_i^a -state population is then reflected in the dissociation signals through the $a^4\Pi_u-f^4\Pi_g$ transition. The first term in Eq. (10) corresponds to the background dissociation signals. The second term is the interference term, which leads to the fine-structure oscillation with frequency of ω_{ij}^{ab} .

One can see from Eq. (10) that the strength of the vibronic QB is proportional to the frequency component $\tilde{\mathbf{E}}(\omega_{ij}^{ab})$ and the initial amplitudes of the vibronic states. Therefore, one can enhance the vibronic QBs from the following two aspects: (i) Enhancing $\tilde{\mathbf{E}}(\omega_{ij}^{ab})$ by manipulating the probe parameters, such as increasing the probe intensity or duration. (ii) Populating the vibronic states with large and comparable amplitudes during the pump ionization. Moreover, the oscillating phase in Eq. (10) consists of two parts: one is the CEP of the probe pulse and the other is the initial phase of the vibronic states $\delta_j^b - \delta_i^a$, which is related to the CEP of the pump pulse. This indicates that the synchronization of the pump and probe CEPs is a necessary condition to observe vibronic QB in the IR-probe scheme. Otherwise, the random phase will make the dissociation signals randomly fluctuate, leading to the loss of subcycle time resolution.

2. QBs upon initial mixed state

Now we investigate the quantum coherences generated by the IR and APT pumps used in the experiments [11,23,24] and the influence of the coherences on QBs.

For the IR case, a 760-nm, 15-fs laser pulse with an intensity of 1.5×10^{14} W/cm² is adopted as the pump. We apply the SFA model to O₂ to calculate the RDM upon ionization. The vibronic DOCs with and without the resonant coupling are shown in Figs. 6(a) and 6(b), respectively. It is found that there are local maxima satisfying $E_j^b - E_i^a \approx \omega$ in both cases. More generally, the vibronic-state pairs with high DOC should satisfy $E_j^b - E_i^a \approx (2n+1)\omega$ due to the opposite parities of the ionization orbitals. When the resonant coupling is considered, the vibronic DOCs become weaker at the range of $v_{i>6}^a$. This can be attributed to the $a^4\Pi_u-b^4\Sigma_g^-$ transition during the pump, which disrupts the periodic coherent condition described in Eq. (6). Despite this apparent irregularity of the local maxima, the local maxima of the vibronic DOCs show a better wavelength-dependent pattern than that of the H₂

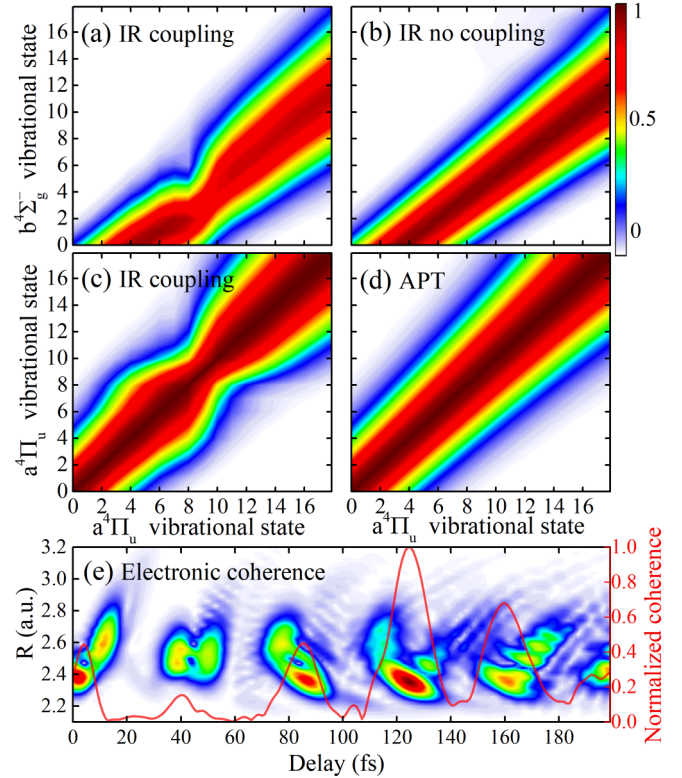


FIG. 6. The degrees of the vibronic coherences g_{ij}^{ab} between states $a^4\Pi_u$ and $b^4\Sigma_g^-$, (a) with and (b) without considering the laser coupling effect for a 15-fs pump pulse with intensity of 1.5×10^{14} W/cm². The degrees of the $a^4\Pi_u$ -state vibrational coherences for the (c) IR and (d) APT pump pulse. (e) Normalized R -dependent electronic coherences (left, y axis) and the total electronic coherence (right, y axis) as a function of the delay time.

model under intense laser field because of the weak transition dipole moment between $a^4\Pi_u$ and $b^4\Sigma_g^-$. Further calculations indicate that the vibronic coherent region hardly changes when the intensities of the pump pulse are in the range of $\sim 10^{13}$ – 10^{15} W/cm². This means that the coherent region remains local even with volume intensity integration. Thus one can simply control the vibronic coherences on O₂⁺ by manipulating the pump wavelength and duration. Figure 6(c) shows the $a^4\Pi_u$ -state vibrational DOCs under the IR pump; the results are similar to the $b^4\Sigma_g^-$ state. It is clear that the vibrational DOC decreases with Δv . This is because the large energy gap will destroy the coherent condition by the periodic ionization bursts that happen during the pump pulse; see the last exponential term in Eq. (6). This is one of the reasons that the high-order vibrational QBs are hard to observe in the experiment.

With the vibronic coherences shown in Fig. 6(a), we further explore the properties of the electronic coherence between $a^4\Pi_u$ and $b^4\Sigma_g^-$. Figure 6(e) presents the R -dependent and normalized total electronic coherences as functions of the delay time. As shown, the electronic coherences are mainly located around $R \sim 2.2$ – 3 a.u. and oscillate with a period of about 40 fs. This can be explained by the oscillations of overlaps between the nuclear wave packets on the $a^4\Pi_u$ and $b^4\Sigma_g^-$ PECs. However, for the H₂ model, the electronic

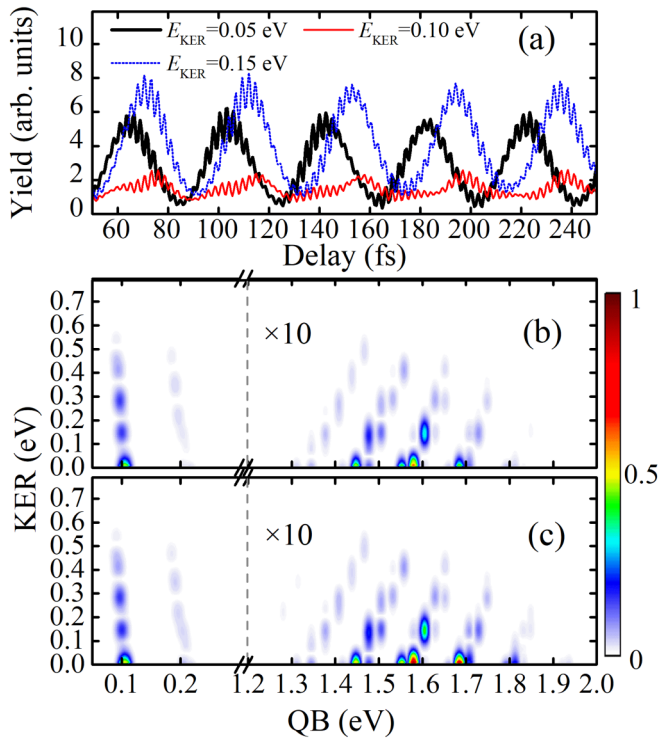


FIG. 7. (a) Ion yields vs time delay at KER near 0.05, 0.1, and 0.15 eV. (b) QB spectrum detected by a 760-nm 15-fs probe pulse with an intensity of 3×10^{12} W/cm². The amplitudes of the vibronic QBs from 1.2 to 2.0 eV are magnified 10 times for a better presentation. The RDM calculated by the SFA model is adopted as the initial condition. (c) Same as (b), but with an initial pure state condition.

coherence between $X^2\Sigma_g^+$ and $A^2\Sigma_u^+$ rapidly drops to zero due to the vanishing overlap of the nuclear wave packets. These two cases support the thesis that the electronic coherence depends on the topology of the PECs relative to each other [20]. To summarize, the molecular electronic coherence, i.e., the oscillatory charge density, is essentially built up by the vibronic coherences generated after photoionization. Therefore, one may control the charge migration and subsequent charge transfer by manipulating the vibronic coherences via photoionization.

For the APT pump, an 8-fs Gaussian envelope is used to mimic the envelope of the APT generated by the 12(3)-fs driving pulse used in the experiment [23]. According to Eq. (9), there is no vibronic coherence between $a^4\Pi_u$ and $b^4\Sigma_g^-$ upon one-photon ionization because of the antisymmetry of the ionization orbitals [14–18]. Therefore, we only give the vibrational DOCs of $a^4\Pi_u$ in Fig. 6(d). The local maxima show a regular diagonal pattern due to the lack of laser coupling.

Using the RDM generated by the IR pump as the initial condition, we calculated the QB spectrum from the delay-dependent KER signals. In the calculation, the 15-fs probe pulse with the intensity of 3×10^{12} W/cm² is adopted. The results are shown in Fig. 7(b). One can see that the strength ratio of the vibronic QBs to the vibrational QBs becomes stronger than that in Fig. 5(c). This is caused by the resonant transition between the vibronic states during the pump pulse, which significantly increases the population of v_j^b . According

to Eq. (10), the comparable vibronic-state populations of v_i^a and v_j^b enhance the strength of the vibronic QB. Moreover, the delay-dependent vibronic oscillations also exhibit good signal contrast (the ratio of fine-structure depth to the background average signal). Especially in the range of $E_{\text{KER}} < 0.2$ eV, the signal contrasts can reach more than 10%. To illustrate this point, delay-dependent signals at three dissociative energies are shown in Fig. 7(a). As discussed in Sec. III B 1, the vibronic QB can be further enhanced by using stronger and longer probe pulses.

To gain insight into the effect of the coherence on the QB, we set the vibrational and vibronic DOCs to 1, which corresponds to the condition of the initial pure state. The calculated QB spectrum is shown in Fig. 7(c). Compared to Fig. 7(b), the QBs do not enhance much. The reason is that the vibronic coherences that can be detected by the probe bandwidth are exactly within the range of the local maxima shown in Fig. 6(a). Further calculations indicate that the vibronic QBs will gradually disappear when the probe wavelength is adjusted away from 760 nm (not shown). Therefore, to observe strong vibronic QBs on O_2^+ , we recommend adopting probe and pump pulses with the same wavelength in experiments.

It should be noted that for the IR pump, one can get almost the same delay-dependence KER spectra when the CEPs of the pump and probe pulses are changed simultaneously in the calculations. However, if the CEP of solely the probe or the pump is changed randomly at each delay time, the delay-dependent fine structures will also fluctuate randomly so that no vibronic QB could be detected. This implies that the CEP synchronization of the pump and probe pulses is a necessary condition to observe a vibronic QB, which agrees with the analysis from Eq. (10).

3. Comparison with experimental data

To compare with the experiments [11,23,24] and further explore the angular properties of the QBs, we calculated the angle-dependent QB spectra, as shown in Fig. 8. For the APT pump case shown in Fig. 8(b), since there is no coherence between $a^4\Pi_u$ and $b^4\Sigma_g^-$, none of the vibronic QB or the $b^4\Sigma_g^-$ -state vibrational QB will show up. The vibrational QBs located at 0.105 eV (25.4 THz) originate solely from the vibrational nuclear motion on the $a^4\Pi_u$ PEC. As can be seen, these signals change slowly with the angle and have no obvious attenuation at small angles ($0.8 < \cos\theta < 1$), which is in good agreement with the angular QB spectrum in Ref. [23].

Unfortunately, for the IR pump case, the dissociation signals are only detected near 90° in the experiments [11,24]. Therefore, we only present a theoretical explanation for the angle-dependent QBs shown in Fig. 8(a). Detailed comparisons with the experiment are discussed in Ref. [25]. For the low-frequency part, the $a^4\Pi_u$ -state vibrational QBs dominate in the spectrum, whereas in the experiments [11,24], the $b^4\Sigma_g^-$ -state vibrational QBs are mainly observed. This is because the probe pulse used in this section is much weaker than that in the experiment ($\sim 10^{14}$ W/cm²), which results in a weak $b^4\Sigma_g^- \rightarrow a^4\Pi_u$ transition. If the probe intensity increases, the $b^4\Sigma_g^-$ -state vibrational QBs will appear. For the high frequency, it can be seen that the positions of the vibronic QBs do not change with the angle. Further calculations indicate

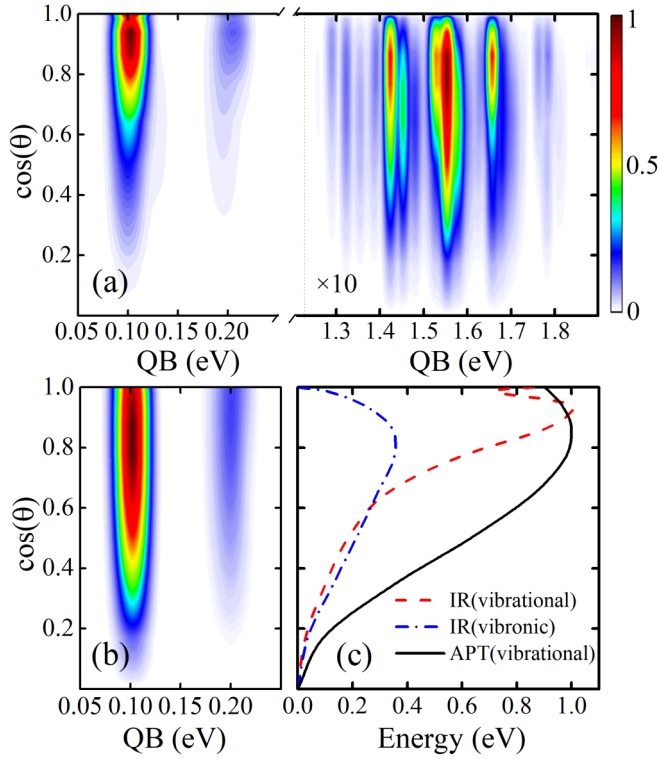


FIG. 8. (a) Angle-dependent vibrational and vibronic QBs for the IR pump pulse detected by the 15-fs probe pulse. The amplitudes of the vibronic QBs from 1.2 to 2.0 eV are magnified 10 times for a better presentation. (b) Angle-dependent vibrational QBs for the APT pump pulse detected by the same 15-fs probe pulse. (c) Angle-dependent integrated signals at low- and high-frequency parts for the IR and APT pump pulses.

that the total delay-dependent KER spectrum still possesses obvious fine-structure oscillations after integrating over all angles (not shown).

To compare the angle-dependent signals more intuitively, we also present the angle-dependent QB signals integrated in the vibrational and vibronic frequency regions in Fig. 8(c). The difference of the vibrational signals between the IR and APT pump cases can be attributed to the $a^4\Pi_u$ -state angular distribution after the pump pulse. It can be seen from Figs. 1(c) and 1(d) that the tunneling ionization results in almost no $a^4\Pi_u$ -state population along 0° , whereas a considerable $a^4\Pi_u$ -state population along 0° is produced by the XUV ionization. For the vibronic QBs in the IR pump case, the signal disappears at 0° and 90° and reaches its maximum around 35° . The main reason is that the transition dipoles of $a^4\Pi_u-b^4\Sigma_g^-$ and $a^4\Pi_u-f^4\Pi_g$ are mutually perpendicular, and the appearance of the vibronic QBs requires a joint contribution of these two transitions.

4. Frequency shift of vibronic QB

The Stark shift is a common phenomenon in atoms and molecules under intense laser fields [36,37]. In principle, the energy shifts of the vibrational states can lead to the frequency shifts of the QBs. In the above sections, the nuclear wave packets prepared after the pump pulse evolve freely in the

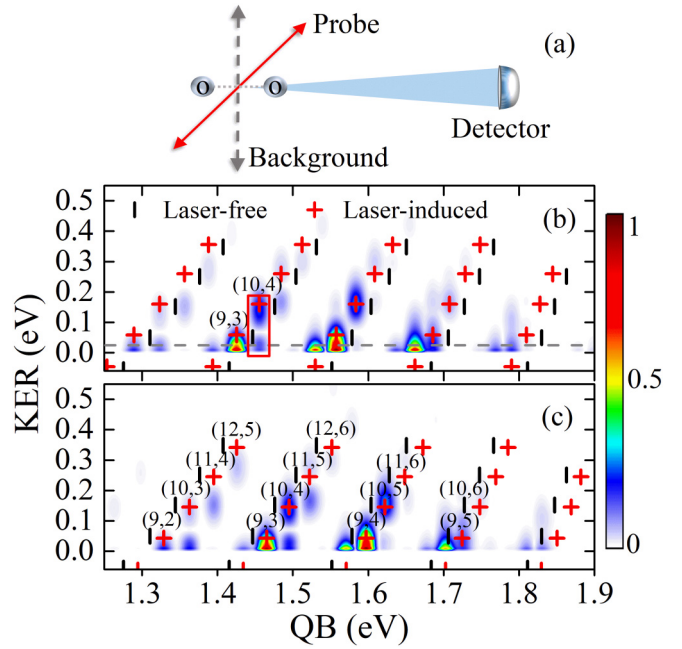


FIG. 9. (a) Diagram of the scheme, setting of the laser polarization directions, and the detection angle. (b) Vibronic QBs under a 400-nm background laser pulse with an intensity of 6×10^{13} W/cm². (c) Vibronic QBs under a 2400-nm background laser pulse with an intensity of 3×10^{13} W/cm². Laser-induced and laser-free vibronic energy differences are shown as red (gray) crosses and black (dark) bars, respectively. Vibronic-state pairs are labeled by (v_i^a, v_j^b) on top of the red (gray) crosses.

basis of the laser-free vibrational states. Therefore, laser-free QBs are detected. To investigate the frequency shifts of the vibronic QBs, we employ a long trapezoidal laser pulse covering the entire delay time as a background field. In this case, the ionic wave packets will evolve in the basis of the laser-induced vibrational states during the delay time, leading to the frequency shifts of the QBs. To simplify the theoretical analysis, the angle between the polarization directions of the background and probe pulses is set to be 45° in our simulations. The diagram of the scheme is depicted in Fig. 9(a). Dissociation signals perpendicular to the polarization direction of the background field are collected so that only the $a^4\Pi_u$ and $b^4\Sigma_g^-$ states are coupled by the background field for the detected molecules.

Figures 9(b) and 9(c) show the vibronic QBs under two different background laser fields. By diagonalizing the Floquet Hamiltonian [38], we obtain the eigenenergies of the laser-induced vibrational states under the background fields. The corresponding vibronic energy differences are marked as red (gray) crosses. For comparison, laser-free vibronic energy differences are marked as black (dark) bars. One can see that the gray (red) crosses accurately match with the QB frequency positions and shift ~ 0.01 – 0.02 eV relative to the black (dark) bars. The frequency shifts can be understood in the Floquet picture [39]. For the 400-nm background field, the Floquet $b^4\Sigma_g^- - \omega$ PEC is slightly lower than the $a^4\Pi_u$ PEC. The dipole coupling makes these two Floquet PECs mutually repel, which means that the laser-induced adiabatic

$a^4\Pi_u$ and $b^4\Sigma_g^-$ PECs get close to each other. This is reflected as the redshifts of the vibronic QBs shown in Fig. 9(b). For the 2400-nm background field, the Floquet $b^4\Sigma_g^- - \omega$ PEC is higher than the $a^4\Pi_u$ PEC. Due to the repelling of the two Floquet PECs, the laser-induced $a^4\Pi_u$ and $b^4\Sigma_g^-$ PECs are farther apart than the laser-free ones, resulting in the blueshifts of the vibronic QBs shown in Fig. 9(c).

One thing that might cause confusion is that there are ~ 2 – 4 peaks around the red (gray) crosses along the horizontal dashed line, and only one peak matches with the theoretical points. This is caused by the probe bandwidth, which gives widths of the KER peaks along the vertical axis, for example (v_{10}^a, v_4^b) shown in the red (gray) box. The redundant peaks can be weakened by using longer probe pulses at a cost of reduction of the vibronic QBs.

In summary, the frequency positions of the vibronic QBs will shift under a long-duration background pulse. By carefully calibrating the QB positions, adiabatic vibrational energies can be effectively extracted, and the laser-induced PECs could be retrieved using procedures such as the semi-classical RKR method.

IV. SUMMARY

We theoretically study the quantum coherence and vibronic QB on an example of O_2 by using the IR(APT)-pump-IR-probe schemes. The SFA and perturbation theory models are used to decide the quantum coherence after photoionization. The validities of the models are tested on a one-dimensional H_2 system. It is found that the vibronic coherence is associated with the inversion symmetries of the ionization orbitals and can be simply controlled by changing the laser parameters. This is due to the symmetry conservation between the initial and final states during the photoionization, which has also been observed in atomic systems [14–18].

The delay-dependent KER and QB spectra are obtained via the numerical solutions of the TDSE and QLE. It is found that the strength of the vibronic QB is proportional to the vibronic-state populations and vibronic coherence. The QB properties are directly influenced by the bandwidth of the probe pulse. Frequency shifts of the vibronic QBs are also investigated under background laser pulses. The laser-induced vibronic states and PECs could be calibrated using the vibronic QBs. In the delay-dependent KER spectra, the depths of the fine-structure oscillations exhibit good contrasts to the background signals even with consideration of angular integration. This provides a good prospect to observe the vibronic QBs in the experimental measurement.

To detect the vibronic coherences in the IR-probe scheme, it is essential to make sure that the CEPs of the pump and probe pulses are synchronized, from which the subcycle resolution is guaranteed. In addition, it is also possible to observe the ultrafast vibronic (or electronic) coherence by using an attosecond pulse as the probe because of its intrinsic attosecond time resolution. In fact, the electronic coherence on Br_2^+ has been observed recently within attosecond transient absorption spectroscopy [40]. However, their method is limited by the symmetries of the electronic states to be probed. Therefore, our method can be complementary since the IR probe can induce a dipole transition between electronic states with different symmetries.

ACKNOWLEDGMENTS

This work was supported by the National Natural Science Foundation of China (NSFC) (Grants No. 11904146, No. 11874030, and No. 12064023), the Natural Science Foundation of Gansu Province (Grant No. 20JR5RA209), and the Scientific Research Program of the Higher Education Institutions of Gansu Province of China (Grant No. 2020A-125).

-
- [1] G. Sansone, F. Kelkensberg, J. Pérez-Torres, F. Morales, M. F. Kling, W. Siu, O. Ghafur, P. Johnsson, M. Svoboda, E. Benedetti, F. Ferrari, F. Lépine, J. L. Sanz-Vicario, S. Zherebtsov, I. Znakovskaya, A. L’Huillier, M. Y. Ivanov, M. Nisoli, F. Martín, and M. J. J. Vrakking, *Nature (London)* **465**, 763 (2010).
 - [2] F. Lépine, M. Y. Ivanov, and M. J. Vrakking, *Nat. Photon.* **8**, 195 (2014).
 - [3] F. Calegari, D. Ayuso, A. Trabattori, L. Belshaw, S. De Camillis, S. Anumula, F. Frassetto, L. Poletto, A. Palacios, P. Decleva, J. B. Greenwood, F. Martín, and M. Nisoli, *Science* **346**, 336 (2014).
 - [4] P. M. Kraus, B. Mignolet, D. Baykusheva, A. Rupenyan, L. Horny, E. F. Penka, G. Grassi, O. I. Tolstikhin, J. Schneider, F. Jensen, L. B. Madsen, A. D. Bandrauk, F. Remacle, and H. J. Wörner, *Science* **350**, 790 (2015).
 - [5] Y. Pertot, C. Schmidt, M. Matthews, A. Chauvet, M. Huppert, V. Svoboda, A. Von Conta, A. Tehlar, D. Baykusheva, J.-P. Wolf, and H. J. Wörner, *Science* **355**, 264 (2017).
 - [6] T. Ergler, A. Rudenko, B. Feuerstein, K. Zrost, C. D. Schröter, R. Moshhammer, and J. Ullrich, *Phys. Rev. Lett.* **97**, 193001 (2006).
 - [7] A. S. Alnaser, B. Ulrich, X. M. Tong, I. V. Litvinyuk, C. M. Maharjan, P. Ranitovic, T. Osipov, R. Ali, S. Ghimire, Z. Chang, C. D. Lin, and C. L. Cocke, *Phys. Rev. A* **72**, 030702(R) (2005).
 - [8] U. Thumm, T. Niederhausen, and B. Feuerstein, *Phys. Rev. A* **77**, 063401 (2008).
 - [9] I. A. Bocharova, A. S. Alnaser, U. Thumm, T. Niederhausen, D. Ray, C. L. Cocke, and I. V. Litvinyuk, *Phys. Rev. A* **83**, 013417 (2011).
 - [10] W. Siu, F. Kelkensberg, G. Gademann, A. Rouzée, P. Johnsson, D. Döwke, M. Lucchini, F. Calegari, U. De Giovannini, A. Rubio, R. R. Lucchese, H. Kono, F. Lépine, and M. J. J. Vrakking, *Phys. Rev. A* **84**, 063412 (2011).
 - [11] S. De, M. Magrakvelidze, I. A. Bocharova, D. Ray, W. Cao, I. Znakovskaya, H. Li, Z. Wang, G. Laurent, U. Thumm, M. F. Kling, I. V. Litvinyuk, I. Ben-Itzhak, and C. L. Cocke, *Phys. Rev. A* **84**, 043410 (2011).
 - [12] M. Magrakvelidze, O. Herrwerth, Y. H. Jiang, A. Rudenko, M. Kurka, L. Foucar, K. U. Kühnel, M. Kübel, N. G. Johnson, C. D. Schröter, S. Dusterer, R. Treusch, M. Lezius, I. Ben-Itzhak, R. Moshhammer, J. Ullrich, M. F. Kling, and U. Thumm, *Phys. Rev. A* **86**, 013415 (2012).

- [13] H. J. Wörner, C. A. Arrell, N. Banerji, A. Cannizzo, M. Chergui, A. K. Das, P. Hamm, U. Keller, P. M. Kraus, E. Liberatore, P. Lopez-Tarifa, M. Lucchini, M. Meuwly, C. Milne, J.-E. Moser, U. Rothlisberger, G. Smolentsev, J. Teuscher, J. A. Van Bokhoven, and O. Wenger, *Struct. Dyn.* **4**, 061508 (2017).
- [14] E. Goulielmakis, Z. Loh, A. Wirth, R. Santra, N. Rohringer, V. S. Yakovlev, S. Zherebtsov, T. Pfeifer, A. M. Azzeer, M. F. Kling, S. R. Leone, and F. Krausz, *Nature (London)* **466**, 739 (2010).
- [15] N. Rohringer and R. Santra, *Phys. Rev. A* **79**, 053402 (2009).
- [16] S. Pabst, L. Greenman, P. J. Ho, D. A. Mazziotti, and R. Santra, *Phys. Rev. Lett.* **106**, 053003 (2011).
- [17] S. Pabst, M. Lein, and H. J. Wörner, *Phys. Rev. A* **93**, 023412 (2016).
- [18] S. Carlström, J. Mauritsson, K. J. Schafer, A. L'Huillier, and M. Gisselbrecht, *J. Phys. B: At. Mol. Opt.* **51**, 015201 (2017).
- [19] M. Vacher, L. Steinberg, A. J. Jenkins, M. J. Bearpark, and M. A. Robb, *Phys. Rev. A* **92**, 040502(R) (2015).
- [20] C. Arnold, O. Vendrell, and R. Santra, *Phys. Rev. A* **95**, 033425 (2017).
- [21] M. Vacher, M. J. Bearpark, M. A. Robb, and J. P. Malhado, *Phys. Rev. Lett.* **118**, 083001 (2017).
- [22] X. Zhang, D. Shi, J. Sun, and Z. Zhu, *Mol. Phys.* **109**, 1627 (2011).
- [23] P. Cörlin, A. Fischer, M. Schönwald, A. Sperl, T. Mizuno, U. Thumm, T. Pfeifer, and R. Moshhammer, *Phys. Rev. A* **91**, 043415 (2015).
- [24] S. De, I. A. Bocharova, M. Magrakvelidze, D. Ray, W. Cao, B. Bergues, U. Thumm, M. F. Kling, I. V. Litvinyuk, and C. L. Cocke, *Phys. Rev. A* **82**, 013408 (2010).
- [25] S. Xue, H. Du, B. Hu, C. D. Lin, and A.-T. Le, *Phys. Rev. A* **97**, 043409 (2018).
- [26] P. Erman and M. Larsson, *Phys. Scr.* **15**, 335 (1977).
- [27] A. Carrington, P. G. Roberts, and P. J. Sarre, *Mol. Phys.* **35**, 1523 (1978).
- [28] C. M. Marian, R. Marian, S. D. Peyerimhoff, B. A. Hess, R. J. Buenker, and G. Seger, *Mol. Phys.* **46**, 779 (1982).
- [29] R. J. Le Roy, *J. Quantum Spectrosc. Radiat. Transf.* **186**, 158 (2017).
- [30] M. Magrakvelidze, C. M. Aikens, and U. Thumm, *Phys. Rev. A* **86**, 023402 (2012).
- [31] S.-F. Zhao, C. Jin, A.-T. Le, T. F. Jiang, and C. D. Lin, *Phys. Rev. A* **81**, 033423 (2010).
- [32] P. Lin and R. R. Lucchese, *J. Chem. Phys.* **116**, 8863 (2002).
- [33] R. E. Goetz, M. Merkel, A. Karamatskou, R. Santra, and C. P. Koch, *Phys. Rev. A* **94**, 023420 (2016).
- [34] J. Yao, S. Jiang, W. Chu, B. Zeng, C. Wu, R. Lu, Z. Li, H. Xie, G. Li, C. Yu, Z. Wang, H. Jiang, Q. Gong, and Y. Cheng, *Phys. Rev. Lett.* **116**, 143007 (2016).
- [35] A. D. Bandrauk and H. Z. Lu, *Phys. Rev. A* **72**, 023408 (2005).
- [36] A. D. Bandrauk and M. L. Sink, *J. Chem. Phys.* **74**, 1110 (1981).
- [37] A. Zavriyev, P. H. Bucksbaum, J. Squier, and F. Saline, *Phys. Rev. Lett.* **70**, 1077 (1993).
- [38] S. Chu, *J. Chem. Phys.* **94**, 7901 (1991).
- [39] A. Giusti-Suzor, X. He, O. Atabek, and F. H. Mies, *Phys. Rev. Lett.* **64**, 515 (1990).
- [40] Y. Kobayashi, D. M. Neumark, and S. R. Leone, *Phys. Rev. A* **102**, 051102(R) (2020).